



Common-cation based Z-scheme ZnS@ZnO core-shell nanostructure for efficient solar-fuel production

Pan Li^{a,b}, Tao He^{a,b,*}

^a CAS Key Laboratory of Nanosystem and Hierarchical Fabrication, CAS Center for Excellence in Nanoscience, National Center for Nanoscience and Technology, Beijing 100190, China

^b University of Chinese Academy of Sciences, Beijing 100049, China

ARTICLE INFO

Keywords:

ZnS@ZnO
Core-shell nanostructure
Z-scheme mechanism
Photocatalysis
Solar fuel

ABSTRACT

Inspired by the nature photosynthesis, fabrication of Z-scheme system is an effective strategy to enhance the photocatalytic activity, via which photogenerated electrons and holes that take part in the redox reactions can be separated spatially and temporally, while their strong redox capability can still be preserved. It is of great importance to construct good Z-scheme demo systems, and yet a considerable challenge to verify the charge transfer direction, which is vital for designing and fabricating the photocatalytic systems with high efficiency. Here ZnS@ZnO core-shell nanostructures were fabricated via simply annealing ZnS(en)_{0.5} precursor, which exhibited superior activity for solar fuel production to ZnS. The Z-scheme mechanism was proposed based on the experimental results of charge transfer study. Direct intimate contact is formed at interface due to in-situ growth with common Zn cation. Specifically, ZnS_xO_{1-x} and/or defects may be formed at the interface, which behave like a mediator in a Z-scheme system. All these account for the observed efficient separation of charge carriers and enhanced activity of photocatalytic reduction.

1. Introduction

Photocatalytic reduction of H₂O and CO₂ into solar fuels like H₂ and CO over semiconductor nanocatalysts is of great significance, as it may mitigate carbon emission and afford alternative energy sources. However, it is noted that the photocatalysts based on a single semiconductor usually show extremely low activity, as it is difficult to exhibit high separation efficiency of charge carriers and wide absorption range. This can be realized by fabricating conventional heterostructure-based photocatalysts (Fig. 1a) [1,2]; while in this case the redox capability of the photogenerated electrons and holes is weakened. Inspired by the nature photosynthesis [3,4], construction of the Z-scheme system is an effective strategy to improve the photocatalytic activity, via which the electrons and holes can be separated spatially and temporally under the premise of keeping their strong redox capability in individual semiconductor (Figs. 1b,c) [1–9]. A variety of Z-scheme systems have been reported hitherto. Typically, two photocatalysts are used in the presence of a suitable redox mediator like Fe³⁺/Fe²⁺ and IO₃[−]/I[−] in the solution [10–15], which can extract electrons from the oxidation catalyst and holes from the reduction catalyst. All-solid-state Z-scheme systems can be fabricated by using noble metals (Au, Ag, etc.) and

graphene as the solid mediator [16,17]. In addition, it is said that no redox mediators exist in the so-called “direct” Z-scheme systems [18–25].

Opposite to the charge-transfer direction mentioned above in the systems with a mediator, it also seems inevitable for the electrons (holes) in the reduction (oxidation) catalysts to react with the mediator, as they exhibit stronger reduction (oxidation) power than those in the oxidation (reduction) catalysts. Definitely, this would counteract the benefits induced by the Z-scheme design. The same concern is true for the “direct” Z-scheme systems since they possess the “same” structure as the type-II conventional heterojunction photocatalysts, i.e., the electrons (holes) may also transfer from the conduction band (CB) (valence band, VB) of the reduction (oxidation) catalysts to that of the oxidation (reduction) catalysts (Fig. 1). So it is critical to fabricate a valid Z-scheme system, in which charge carriers transfer along the expected direction. The electrons in the reduction catalyst can indeed take part in the reduction reactions for some Z-scheme systems, such as CdS/WO₃ [26], SnO₂–x/g-C₃N₄ [27], g-C₃N₄/WO₃ [28], α-Fe₂O₃/Cu₂O [29] and Ag₃PO₄/g-C₃N₄ [30], as the CB potential of the oxidation catalyst seems not negative enough to reduce the CO₂. However, it is very common that the CB potential for both the reduction and oxidation

* Corresponding author at: CAS Key Laboratory of Nanosystem and Hierarchical Fabrication, CAS Center for Excellence in Nanoscience, National Center for Nanoscience and Technology, Beijing 100190, China.

E-mail address: het@nanoctr.cn (T. He).

<https://doi.org/10.1016/j.apcatb.2018.07.057>

Received 5 February 2018; Received in revised form 8 May 2018; Accepted 20 July 2018

Available online 22 July 2018

0926-3373/ © 2018 Elsevier B.V. All rights reserved.

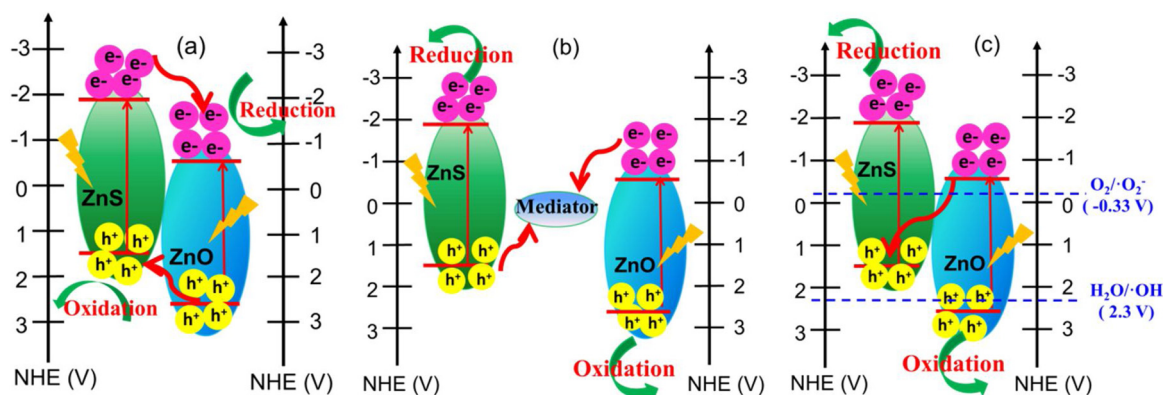
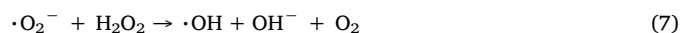


Fig. 1. Schematic illustration of charge transfer for the heterojunctions in terms of different mechanism, (a) type II conventional heterojunction, (b) Z scheme with a mediator, and (c) “direct” Z scheme. Here ZnS and ZnO are used to represent the reduction and oxidation catalysts, respectively.

catalysts in a Z-scheme system is negative enough, such as ZnO/g-C₃N₄ [31], CdS/TiO₂ [32] and g-C₃N₄/Bi₂WO₆ [33]. In this case, solid evidence should be provided to confirm the charge-transfer direction.

It is noted that direct oxidation of H₂O or OH[−] by the holes photogenerated in the VB of a semiconductor can lead to formation of the hydroxyl radicals ($\cdot\text{OH}$) (Eqs. (1) and (2)), and the direct reduction of O₂ by the electrons generated in the CB of a semiconductor can produce the superoxide radicals ($\cdot\text{O}_2^-$) (Eq. (3)). Electron spin resonance (ESR) is usually used to probe the formation of the radicals. Thus, here 5,5-dimethylpyrroline N-oxide (DMPO) is employed to react respectively with the $\cdot\text{OH}$ and $\cdot\text{O}_2^-$ radicals so as to form DMPO- $\cdot\text{OH}$ and DMPO- $\cdot\text{O}_2^-$, giving rise to different features in the ESR spectra [34,35]. In addition, photoluminescence (PL) method using terephthalic acid (TA) as the probe molecule can be used too, as the TA can quickly react with the $\cdot\text{OH}$ radical to produce a highly fluorescent product (2-hydroxyterephthalic acid) that exhibits a PL peak at 425 nm with 315 nm light excitation [36]. However, it is known that the $\cdot\text{OH}$ radical can also be produced via a series reactions after the $\cdot\text{O}_2^-$ radical and/or H₂O₂ is formed upon the reduction of O₂ by electrons (Eqs. (4)–(8)), not only from the direct oxidation of H₂O or OH[−] by the photogenerated holes (Eqs. (1)–(3)). All these make it difficult to study the behavior of both photogenerated electrons and holes, thereby, very challenging to determine the charge-transfer direction.



Herein we fabricated Z-scheme nanostructures using ZnO and ZnS. Unlike those reported previously that the CB potential of oxidation catalysts is not negative enough to reduce the CO₂, in this work the CB potential for both catalysts is negative enough, while the VB potential of the reduction catalyst (i.e., ZnS) is not positive enough to oxidize OH[−] and/or H₂O to form the $\cdot\text{OH}$ radical. Thus, this system is in favor of probing the behavior of photogenerated holes if the amount of O₂ in the system can be minimized, as the $\cdot\text{OH}$ radicals are formed overwhelmingly from the direct oxidation of H₂O or OH[−] by the holes. Moreover, porous ZnS@ZnO core-shell nanostructure was prepared by in-situ growth of ZnO directly on the ZnS surface via simply annealing the as-prepared ZnS(en)_{0.5} precursor in air. The interface formed by a

chemical approach is believed to be more effective for charge transfer than that via a physical approach [1]. Especially, the common cation in the two constituents can also play an important role. The Z-scheme mechanism of charge transfer was verified by the ESR and PL measurements. Accordingly, the obtained ZnS@ZnO core-shell nanostructures exhibit superior activity to pure ZnS for solar fuel production.

2. Experimental section

2.1. Chemicals

All the chemicals were analytical reagent and were used without any further purification. Zinc powder (AR) and ethylenediamine (> 99%) were bought from Shanghai Aladdin biological technology co., LTD. Sulfur powder and absolute ethanol (≥99.7%) were purchased from Beijing Chemical Works. Pure water used in the experiment was made by a Milli-Q Plus system (Millipore, France) with 18.2 MΩ cm resistivity.

2.2. Preparation of ZnS(en)_{0.5} precursor

ZnS(en)_{0.5} precursor was synthesized according to the previous report via a solvothermal route in the presence of ethylenediamine (en) as solvent and structure-directing agent with minor modification [37]. In the typical process, 1 mmol Zn powder and 3 mmol S powder were dissolved in 90 mL of ethylenediamine under constant stirring for half an hour. Subsequently, the mixture was transferred into an autoclave, which was then put into a furnace and maintained at 180 °C for 24 h. After the autoclave naturally cooled down to room temperature, the resultant white precipitate was separated by centrifugation, and was washed thereafter with ethanol and pure water for several times so as to remove the residuals like organic solvent. The obtained product was finally dried overnight at 65 °C in vacuum oven.

2.3. Preparation of ZnS@ZnO core-shell nanostructures

The ZnS@ZnO core-shell nanostructures were prepared via a simple thermal treatment of as-synthesized ZnS(en)_{0.5} using previously reported protocol with some modifications [38,39]. Typically, the constitution ratio of the two materials in the core-shell structure can be easily tuned by annealing the as-prepared ZnS(en)_{0.5} precursor at 500 °C in air for different time (0.5, 1, 2, 4, and 6 h), which were denoted as ZnS@ZnO-0.5 h, ZnS@ZnO-1 h, ZnS@ZnO-2 h, ZnS@ZnO-4 h, ZnS@ZnO-6 h, respectively. Pure ZnS was synthesized by annealing ZnS(en)_{0.5} precursor in Ar at 400 °C for 2 h. Pure ZnO was prepared by annealing ZnS(en)_{0.5} precursor in air at 600 °C for 2 h.

2.4. Characterization techniques

The crystal structure of the obtained products was identified from 20 to 80° at a scan rate of 0.1 s/step by X-ray diffraction (XRD) using Bruker D8 focus diffractometer with Cu-K α radiation. Fourier transform infrared (FTIR) absorption spectra were carried out on a Perkin Elmer spectrometer from 4500 to 500 cm⁻¹. Thermogravimetric (TG) analysis was conducted with a flow rate of 200 mL/min and a heating rate of 10 °C/min in air by Diamond TG/DTA thermal analyzer. UV–vis diffuse reflectance spectra were collected by Lambda 750 UV–Vis/NIR spectrophotometer using BaSO₄ as the background. The surface morphology and lattice structure of the as-prepared samples were visualized by using Hitachi S4800 field-emission scanning electron microscopy (FE-SEM) and Tecnai G2 F20 U-TWIN transmission electron microscopy (TEM). The BET specific surface area and CO₂ adsorption isotherm spectra were obtained by a surface area and porosity analyzer (Micromeritics, Tristar II 3020). The VB position of the products was measured with X-ray photoelectron spectroscopy (XPS) using ESCALAB 250Xi X-ray photoelectron spectrometer. Electron spin resonance (ESR) signals of spin-trapped paramagnetic radicals with 5,5-dimethyl-pyrroline N-oxide (DMPO) were recorded with a Bruker E500 spectrometer at room temperature. Photoluminescence (PL) spectra were collected on a NanoLOG-TCSPC spectrophotometer (HORIBA JOBIN YVON) with an excitation wavelength of 315 (for radical detection) and 350 nm (for collecting steady state PL spectra) at room temperature. The time-resolved PL spectra were recorded on spectrometer (FLS920, Edinburgh Instruments) with an excitation wavelength of 375 nm.

2.5. Photocatalytic reduction of CO₂

The photoreduction of CO₂ was conducted in a quartz reactor illuminated by a 300-W Xe lamp (PLS-SXE300) with UV–vis light under constant stirring. For the photocatalytic measurements, CO₂ was first bubbled into 100 mL of 1 M NaOH solution for at least 30 min. Then 30 mg of ZnS@ZnO powder was suspended in the above solution under sonication for 30 min. Finally, pure compressed CO₂ ($\geq 99.999\%$) was bubbled into the suspended solution for another 30 min in the dark to achieve the equilibrium of CO₂ absorption-desorption before the illumination. The products were collected every half an hour and analyzed online by gas chromatograph (Agilent 7890 A) equipped with flame ionization detector (FID) and thermal conductivity detector (TCD).

3. Results and discussion

3.1. Structure and morphology

The FTIR technique is used to study whether or not the ethylenediamine used during the sample synthesis is completely removed upon precursor annealing (Fig. 2). The peaks for ZnS(en)_{0.5} precursor appearing at 3240 and 3120 cm⁻¹ are attributed to stretching vibration of –NH₂, and the one at 640 cm⁻¹ is assigned to the wagging vibration of –NH₂ [40]. The peaks at 2940 and 2870 cm⁻¹ are ascribed to the –CH₂ stretching vibration. The peaks at 1600 and 1355 cm⁻¹ represent the scissoring vibration of –NH₂ and –CH₂, respectively. In addition, the peaks at 1080 and 1030 cm⁻¹ are assigned to the stretching vibration of C–C and C–N, respectively [40]. Obviously, all of the aforementioned peaks cannot be observed in the FTIR spectra of the samples upon annealing ZnS(en)_{0.5} precursor at 500 °C for different time, indicating the complete removal of ethylenediamine in the obtained samples. Thus, pure inorganic nanomaterials are obtained after the thermal annealing of ZnS(en)_{0.5}, which can be further confirmed by the XRD results.

The XRD patterns of different samples prepared by annealing ZnS(en)_{0.5} at 500 °C for different time are shown in Fig. 3. It can be seen that pure ZnS is formed after the thermal treatment for 0.5 h since all the diffraction peaks agree well with standard wurtzite-2H structure of ZnS (JCPDS No. 36-1450, *a* = 0.382 nm, *c* = 0.626 nm). The peaks of

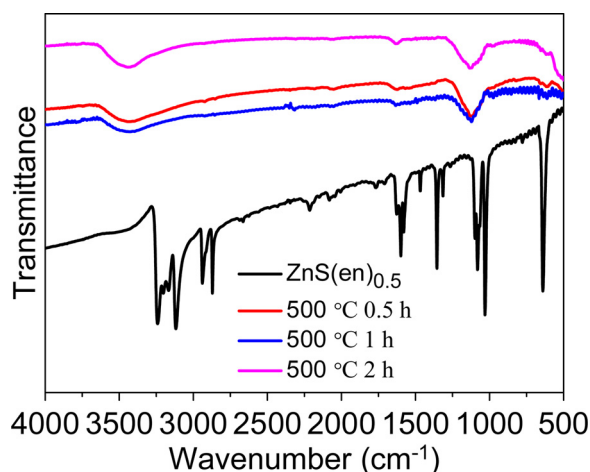


Fig. 2. FTIR spectra of ZnS(en)_{0.5} precursor and the as-prepared samples by annealing ZnS(en)_{0.5} at 500 °C for different time.

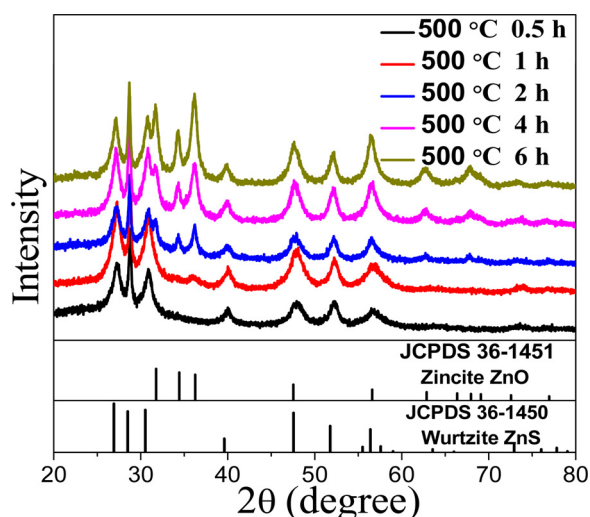


Fig. 3. XRD patterns of as-prepared samples by annealing ZnS(en)_{0.5} at 500 °C for different time.

ZnO can be observed after thermal annealing for 1 h, as all the diffraction peaks are consistent with the standard zincite ZnO (JCPDS No. 36-1451, *a* = *b* = 0.325 nm, *c* = 0.521 nm). The peaks of ZnO become more and more evident when the annealing time is further prolonged, indicating that the amount of ZnO in the products is increasing. No other peaks can be observed in all the samples after calcination, implying the complete removal of ethylenediamine, as indicated by the FTIR results (Fig. 2). The amount of ZnO in ZnS@ZnO-0.5 h, ZnS@ZnO-1 h, ZnS@ZnO-2 h, ZnS@ZnO-4 h and ZnS@ZnO-6 h can be determined approximately according to thermogravimetric (TG) results (Fig. S1), which is ~ 0%, 3.2%, 14.6%, 24.2% and 36.0%, respectively. So the amount of ZnO becomes larger and larger with increase of annealing time, which is consistent with the above XRD results. Similar results can also be obtained from the EDX measurements (Table S1). This is reasonable since the thermal oxidation undergoes continuously with annealing. That no ZnO is observed in ZnS@ZnO-0.5 h is possibly because its amount is beyond the detection limit of TG technique.

SEM images of the obtained samples are shown in Fig. 4. ZnS(en)_{0.5} precursor exhibits sheet-like morphology and smooth surface (Fig. 4a). Although the sheet-like morphology can be maintained during annealing, the surface becomes more and more rough with increasing annealing time (Fig. 4b–e). Such porous nature can be further confirmed by TEM image (Fig. 5). Moreover, both the diffraction spots of

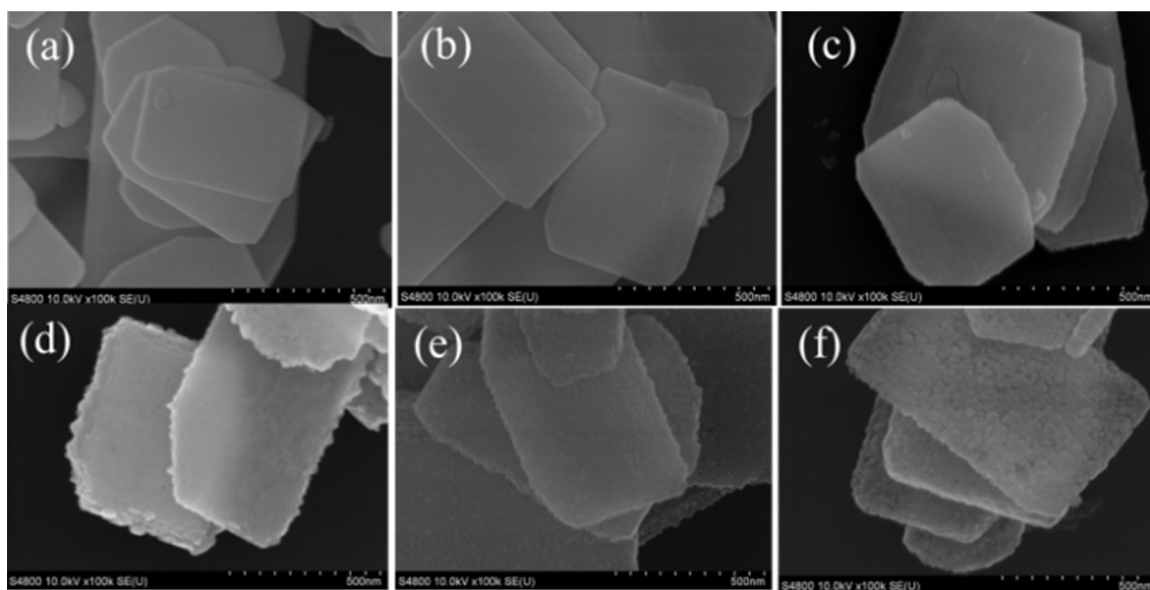


Fig. 4. SEM images of (a) $\text{ZnS(en)}_{0.5}$, (b) ZnS@ZnO-0.5 h , (c) ZnS@ZnO-1 h , (d) ZnS@ZnO-2 h , (e) ZnS@ZnO-4 h , and (f) ZnS@ZnO-6 h .

ZnO (yellow line) and ZnS (red line) can be seen undoubtedly in the SAED pattern. Thus, again, it is concluded that ZnS and ZnO co-exist in the annealed sample. Specifically, EDX mapping indicates that the core-shell structure is well formed for the sample being annealed for 4 h; while it is destroyed and becomes blurred if the annealing time increases to 6 h (Fig. S2). It is noted that the ZnS@ZnO core-shell structure with a thinner shell is obtained if it is annealed for 2 h (Fig. S3). When the annealing time further decreases to 1 h, however, the core-shell structure is not well formed, albeit ZnO still coexists with ZnS (Figs. 5 and S4).

3.2. Photocatalytic reduction of CO_2

The results of photocatalytic reduction are shown in Fig. 6. The

control experiment without CO_2 but just in Ar is carried out first before CO_2 reduction. No products such as CH_4 and CO are observed, confirming the absence of carbon contamination in our system. Thus, CO_2 is the only carbon source for any potential reduction products. It is found that CO is the major product of CO_2 photoreduction, plenty of H_2 is evolved owing to competitive reaction of water splitting. No H_2 can be observed over ZnO , while $\sim 0.21 \text{ mmol/g}$ yield is observed over ZnS after 5-h irradiation. When ZnS is coated with ZnO , the H_2 yield is further improved. The longer the annealing time at 500°C , the higher the H_2 yield is. The highest H_2 yield of $\sim 0.73 \text{ mmol/g}$ after 5-h irradiation is observed over ZnS@ZnO-4 h . The same trend of photocatalytic activity is observed for CO_2 reduction. ZnS@ZnO-4 h shows the highest activity for CO production, followed by $\text{ZnS@ZnO-2 h} > \text{ZnS@ZnO-1 h} > \text{ZnS} > \text{ZnO}$. The mechanism accounting for the

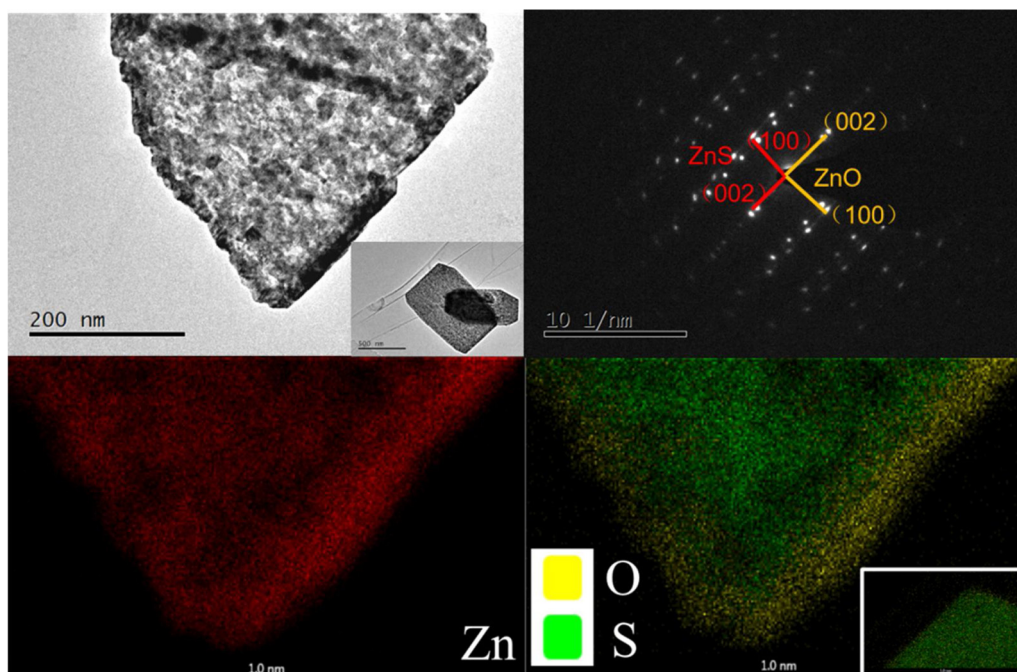


Fig. 5. TEM image, SAED pattern and EDX mapping of ZnS@ZnO-4 h sample. Insets in the bottom right corner of the TEM image and mapping of O and S elements are those for ZnS@ZnO-1 h sample. (For interpretation of the references to colour in the figure text, the reader is referred to the web version of this article).

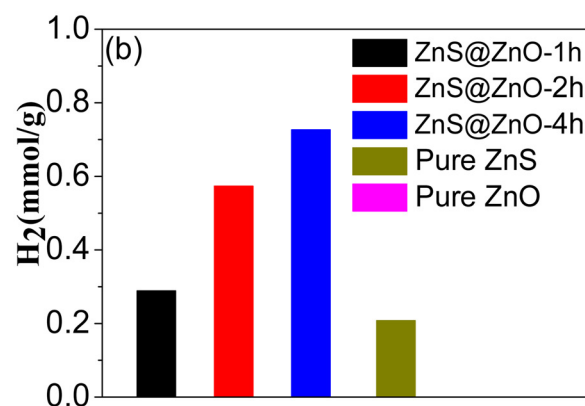
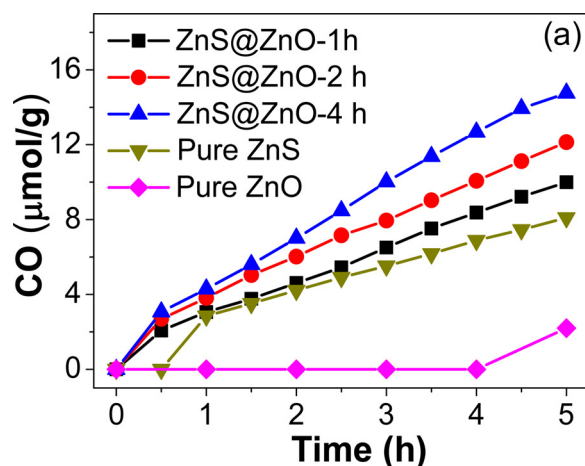


Fig. 6. (a) CO and (b) H₂ evolution using the obtained ZnS, ZnO and ZnS@ZnO nanostructure as the photocatalysts after 5-h irradiation.

observed difference in the photocatalytic activity is given below.

It is noted that the photocatalytic activity of a photocatalyst relies on light harvesting, separation of charge carriers, and CO₂ adsorption. According to the typical N₂ adsorption-desorption isotherm of the as-prepared ZnS@ZnO nanostructures (Fig. S5), the BET specific surface area of ZnS@ZnO-1 h, ZnS@ZnO-2 h and ZnS@ZnO-4 h is determined to be ~24.4, 30.1 and 33.5 m² g⁻¹, respectively. Although the specific surface area of different ZnS@ZnO samples increases slightly with increased annealing time due to the marginally increased porosity as evidenced by SEM results (Fig. 4), they exhibit almost the same CO₂ adsorption capability (Fig. S6). Moreover, the results of UV–vis diffuse reflectance spectra indicate that almost no change in the absorption edge can be observed among different ZnS@ZnO samples (Fig. S7, ~3.20 eV), which roughly corresponds to the band gap of ZnO. In addition, energy level of ZnS@ZnO (pseudo-VB and pseudo-CB) shifts downward by ~0.2–0.3 eV when annealing time increases from 1 h to 2 h, and further to 4 h (Figs. S8 and S9), indicating that the contribution from ZnO becomes more and more. Furthermore, lower CB position means less reduction power of the photogenerated electrons. Such a change trend is opposite to that observed in the catalytic activity. Thus, it is believed that the separation of charge carriers may play a major role in the observed photocatalytic activity of the obtained samples.

The photocatalytic activity can be enhanced greatly once a proper heterojunction can be formed in a catalytic system due to efficient charge separation [24,25]. This is usually evidenced by time-resolved fluorescence decay measurements, from which the PL lifetime can be determined. The decay curves measured using the emission wavelength determined by the PL spectra (Fig. S10) are fitted mathematically by tri-

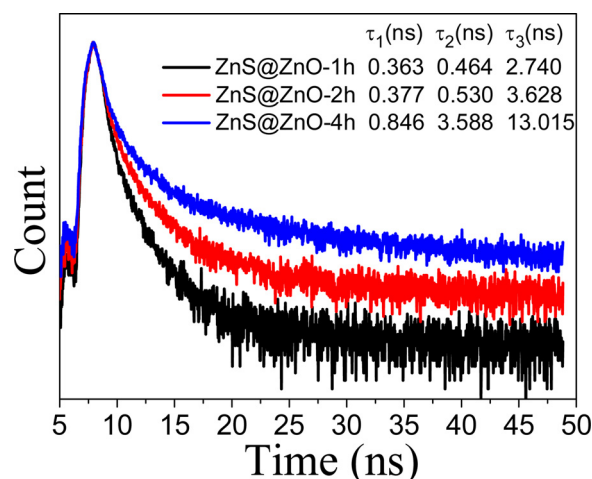


Fig. 7. Time-resolved fluorescence decay curves of the as-synthesized ZnS@ZnO samples measured with an emission wavelength of 500 nm.

exponential decay kinetics (Fig. 7). The PL lifetime includes three processes, short lifetime component (τ₁) owing to non-radiative process, medium long one (τ₂) due to radiative process related to the recombination of photogenerated electrons and holes, and long lifetime one (τ₃) from energy transfer process. The ZnS@ZnO-4 h exhibits the longest lifetime of τ₂, followed by ZnS@ZnO-2 h, and ZnS@ZnO-1 h is the shortest, indicating enhanced separation of charge carriers (i.e., suppressed recombination) with increased annealing time. This agrees well with the sequence of photocatalytic activity.

3.3. Probing the Z-scheme mechanism

Once upon the ZnS@ZnO heterostructure is irradiated with UV light, electrons will be excited to the CB of ZnS and ZnO, while holes are left in the VB. The charge transfer can occur between ZnS and ZnO in ZnS@ZnO due to Fermi level difference and direct intimate contact between them, leading to the above efficient separation of charge carriers. Here the ESR and PL techniques are used to probe the related charge transfer, specifically the validity of Z-scheme mechanism. The O₂ in the system is removed by Ar purging before the two measurements so as to minimize the influence of ·O₂⁻ radical due to the reaction of O₂ with photogenerated electrons.

ESR spectra measured in anaerobic atmosphere are shown in Fig. 8a, of which the signals for ZnS and ZnS@ZnO are magnified by 20 times so as to be observed clearly. The characteristic peaks of DMPO·O₂⁻ with a standard intensity ratio of 1:1:1:1 can be observed for pure ZnS, though very weak, which may result from the reaction of photogenerated electrons with trace amount of O₂. Moreover, water or OH⁻ cannot be oxidized by the holes in ZnS to generate ·OH since its potential is not positive enough, as confirmed by the absence of DMPO·OH signal. However, strong peaks with a standard intensity ratio of 1:2:2:1 are observed when ZnO is used as the photocatalyst, which is ascribed to the formation of DMPO·OH. This strong signal indicates that the ·OH radical is produced only via the oxidation of water or OH⁻ by the holes in ZnO, as there is little amount of ·O₂⁻ radical that are consumed by DMPO. As for the ZnS@ZnO, it is found that the peak position is almost the same as that of pure ZnO while slightly different from that of ZnS, albeit with an intensity ratio deviated slightly from 1:2:2:1, which is possibly due to the interference of trace amount of DMPO·O₂⁻. This signal is quite weak mainly because the amount of ZnO in the ZnS@ZnO is very low. Thus, the holes first accumulate in the VB of ZnO for the ZnS@ZnO and then oxidize water or OH⁻ to generate ·OH radicals. This strongly suggests that charge transfer in the core-shell structure follows the Z-scheme mechanism (Fig. 1), i.e., the electrons generated in ZnO can recombine with the holes generated in ZnS.

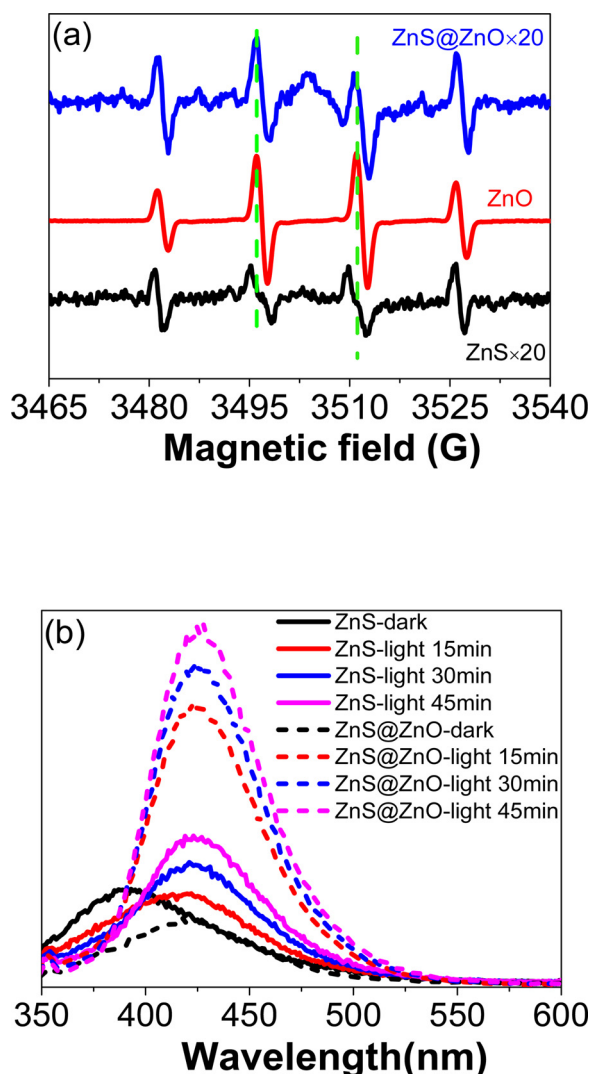


Fig. 8. (a) ESR spectra, and (b) PL spectra observed during illumination for ZnS (solid line) and ZnS@ZnO-2 h (dash line) in 2×10^{-3} M NaOH solution in the presence of 5×10^{-4} M TA of the ZnS, ZnO and ZnS@ZnO-2 h samples.

PL spectra is used to further verify the Z-scheme mechanism for ZnS@ZnO. When the photocatalysts are excited by the light with a wavelength of 315 nm, the peak at 425 nm is used as the probe for the formation of $\cdot\text{OH}$ radicals (Fig. 8b). It is noted that trace amount of O_2 always exists in the system even it is purged thoroughly with Ar during the measurements, which can react with the photogenerated electrons to produce $\cdot\text{O}_2^-$ radicals, leading to the formation of $\cdot\text{OH}$ radicals eventually (Eqs. (3)–(8)). This explains well why a weak peak still appears at 425 nm for ZnS, although the oxidation potential of photogenerated holes in ZnS is not positive enough. Furthermore, a strong peak at 425 nm is observed for ZnS@ZnO. It is found that the peak intensity for both ZnS and ZnS@ZnO samples increases with increasing illumination duration. Considering the amount of ZnS in ZnS@ZnO used for the PL measurements is slightly less than that of pure ZnS and the amount of O_2 is extremely low in the system, it is believed that the formation of $\cdot\text{OH}$ for the system containing ZnS@ZnO is indeed due to the oxidation of water or OH^- by the holes generated in the VB of ZnO since the peak intensity for ZnS@ZnO is much stronger than that for ZnS.

If the charge transfer follows the conventional heterojunction mechanism for the ZnS@ZnO (Fig. 1a), however, the holes accumulated in the VB of ZnS are not able to oxidize water or OH^- to produce $\cdot\text{OH}$, for which the observed signal arises from the series reactions of O_2 with

electrons accumulated in the CB of ZnO. It is noted that the potential of CB level for ZnO is less negative than that for ZnS, also considering the fact that there is very little amount of O_2 in the system, the corresponding PL signal for the ZnS@ZnO would be very weak, or at least similar to that for ZnS; while this is just opposite to the above experimental results. In addition, the charge transfer rate may be faster at the solid/solid interface than that of solid/liquid. So it is concluded that the charge transfer follows the Z-scheme mechanism for ZnS@ZnO (Figs. 1b,c), which agrees well with the ESR results discussed above.

Furthermore, since the common cation of Zn is present in the ZnS@ZnO and the lattice mismatch between them is about 15%, a direct intimate contact can be formed at the interface of ZnS and ZnO. Though it is extremely difficult to directly characterize the constitution and structure at the interface region, it is suggested that the $\text{ZnS}_x\text{O}_{1-x}$ may be formed at the interface, which can be similar to, if not, a solid solution that can act as a mediator, through which the charge carriers can be trapped. Moreover, the defects like sulfur and/or oxygen vacancy may be formed at the interface as well, which can also trap the charge carriers [41,42]. Nevertheless, the nascent $\text{ZnS}_x\text{O}_{1-x}$ and/or defects at the interface can behave like a mediator, via which the electrons generated in the CB of ZnO can recombine with the holes produced in the VB of ZnS (Fig. 9). This may explain why the Z-scheme mechanism works in the ZnS@ZnO nanostructure.

Thus, the solar fuel production over the ZnS@ZnO nanostructures via Zscheme mechanism can be briefly explained in terms of Fig. 9. The electrons are first excited to the respective CB of ZnS and ZnO upon irradiation, and the holes are left in the respective VB accordingly. Then the electrons in the CB of ZnO will recombine with the holes in the VB of ZnS; meanwhile the electrons in the CB of ZnS take part in the reduction reaction of CO_2 and/or water (CO and H_2 evolution, respectively) and the holes in the VB of ZnO participate in the oxidation of water (O_2 evolution and/or other oxygen-containing species like adsorbed oxygen on the surface), without losing the respective redox power. The nature of ZnS nanomaterial may account for that the H_2 evolution is much more than that of CO , which needs further study.

In addition, as manifested in Fig. 6, the ratio of reduction and oxidation photocatalyst in a core-shell ZnS@ZnO Z-scheme nanostructure also plays an important role in the photocatalytic activity. First of all, the chemical species involved in the redox reactions should be able to freely cross the ZnO shell. For this concern, it is better for the shell material to be porous in nature, which is exactly the case in our work (Figs. 4 and 5). Moreover, suitable ZnO shell is required to form the target heterojunction so as to achieve efficient charge transfer at the interface. Ideally, the number of electrons generated in the CB of ZnO

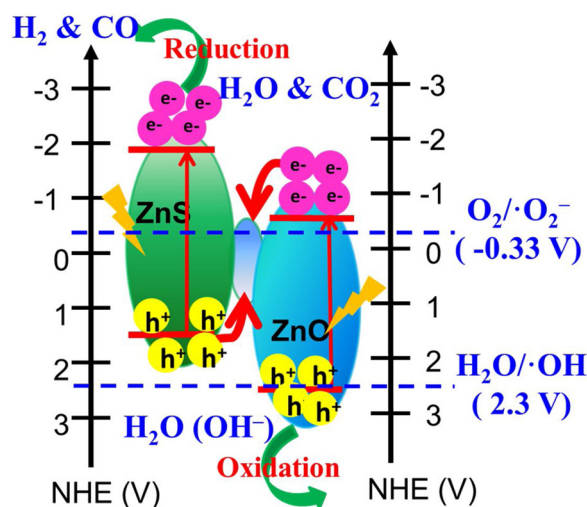


Fig. 9. Proposed Z scheme mechanism for the solar fuel production over the obtained ZnS@ZnO core-shell nanostructures.

should be precisely equal to that of the holes formed in the VB of ZnS. So the activity would be very low if the amount of ZnO in the core-shell structure is not high enough. Here the optimized system is ZnS@ZnO-4 h, as a longer annealing time like 6 h would lead to a totally different morphology (Fig. S2), though it can result in the formation of ZnO shell with a larger amount that may be in favor of photocatalysis.

4. Conclusions

In conclusion, the ZnS@ZnO core-shell nanostructures were successfully fabricated through an in-situ growth of ZnO on ZnS via a simple thermal treatment of as-prepared ZnS(en)_{0.5} in air. According to the ESR and PL results, the electrons generated in the CB of ZnO can recombine with the holes produced in the VB of ZnS. Albeit no solid evidence can be provided in literature or this work that the validity of type-II heterojunction mechanism can be absolutely excluded, the experimental results reported here do indicate that the Z-scheme mechanism is indeed valid in the obtained ZnS@ZnO samples and play a very important role in the photocatalysis, leading to superior activity to ZnS for the reduction of H₂O and CO₂. The interface, here the proposed ZnS_xO_{1-x} and/or defects that need to be further clarified, plays a vital role in the proposed mechanism. It is envisioned that this work can afford a better understanding about the design and fabrication of the Z-scheme photocatalysts with high efficiency for solar fuel production.

Acknowledgments

This work was financially supported by the Ministry of Science and Technology of China (2015DFG62610), and the Belt and Road Initiative by Chinese Academy of Sciences.

Appendix A. Supplementary data

Supplementary material related to this article can be found, in the online version, at doi:<https://doi.org/10.1016/j.apcatb.2018.07.057>.

References

- [1] H. Li, W.G. Tu, Y. Zhou, Z.G. Zou, *Adv. Sci.* 3 (2016) 1500389.
- [2] P. Zhou, J.G. Yu, M. Jaroniec, *Adv. Mater.* 26 (2014) 4920–4935.
- [3] T. Kothé, N. Plumere, A. Badura, M.M. Nowaczyk, D.A. Guschin, M. Rogner, W. Schuhmann, *Angew. Chem. Int. Ed.* 52 (2013) 14233–14236.
- [4] A.J. Bard, M.A. Fox, *Acc. Chem. Res.* 28 (1995) 141–145.
- [5] H. Li, Y. Zhou, W.G. Tu, J. Ye, Z.G. Zou, *Adv. Funct. Mater.* 25 (2015) 998–1013.
- [6] Y. Tachibana, L. Vayssieres, J.R. Durrant, *Nat. Photon.* 6 (2012) 511–518.
- [7] J. Low, C. Jiang, B. Cheng, S. Wageh, A.A. Al-Ghamdi, J.G. Yu, *Small Methods* 1 (2017) 1700080.
- [8] P. Li, H.J. Li, W.G. Tu, Y. Zhou, Z.G. Zou, *Acta Phys. Sin.* 64 (2015) 094209.
- [9] K. Li, B. Peng, T.Y. Peng, *ACS Catal.* 6 (2016) 7485–7527.
- [10] Y. Sasaki, A. Iwase, H. Kato, A. Kudo, *J. Catal.* 259 (2008) 133–137.
- [11] R. Abe, K. Shinmei, N. Koumura, K. Hara, B. Ohtani, *J. Am. Chem. Soc.* 135 (2013) 16872–16884.
- [12] Y. Sasaki, H. Kato, A. Kudo, *J. Am. Chem. Soc.* 135 (2013) 5441–5449.
- [13] K.K. Sakimoto, S.J. Zhang, P.D. Yang, *Nano Lett.* 16 (2016) 5883–5887.
- [14] Y. Miseki, S. Fujiyoshi, T. Gunji, K. Sayama, *J. Phys. Chem. C* 121 (2017) 9691–9697.
- [15] K. Sayama, R. Abe, H. Arakawa, H. Sugihara, *Catal. Commun.* 7 (2006) 96–99.
- [16] H. Tada, T. Mitsui, T. Kiyonaga, T. Akita, K. Tanaka, *Nat. Mater.* 5 (2006) 782–786.
- [17] H. Li, Y. Gao, Y. Zhou, F. Fan, Q. Han, Q. Xu, X. Wang, M. Xiao, C. Li, Z.G. Zou, *Nano Lett.* 16 (2016) 5547–5552.
- [18] Z.F. Huang, J.J. S. X. Wang, L. Pan, K. Li, X.W. Zhang, L. Wang, J.J. Zou, *Nano Energy* 40 (2017) 308–316.
- [19] Z. Zhang, J. Huang, Y. Fang, M. Zhang, K. Liu, B. Dong, *Adv. Mater.* 29 (2017) 1606688.
- [20] B. Qiu, Q. Zhu, M. Du, L. Fan, M. Xing, J. Zhang, *Angew. Chem. Int. Ed.* 56 (2017) 2684–2688.
- [21] Q. Yuan, D. Liu, N. Zhang, W. Ye, H. Ju, L. Shi, R. Long, J. Zhu, Y.J. Xiong, *Angew. Chem. Int. Ed.* 56 (2017) 4270–4274.
- [22] K.H. Cho, Y.M. Sung, *Nano Energy* 36 (2017) 176–185.
- [23] Z. Huang, Q. Sun, K. Lv, Z. Zhang, M. Li, B. Li, *Appl. Catal. B* 164 (2015) 420–427.
- [24] J. Low, J.G. Yu, M. Jaroniec, S. Wageh, A.A. Al-Ghamdi, *Adv. Mater.* 29 (2017) 1601694.
- [25] L.J. Guo, Y.J. Wang, T. He, *Chem. Rec.* 16 (2016) 1918–1933.
- [26] J. Jin, J. Yu, D. Guo, C. Cui, W. Ho, *Small* 11 (2015) 5262–5271.
- [27] Y. He, L. Zhang, M. Fan, X. Wang, M.L. Wallbridge, Q. Nong, Y. Wu, L. Zhao, *Sol. Energy Mater. Sol. Cells* 137 (2015) 175–184.
- [28] T. Ohno, N. Murakami, T. Koyanagi, Y. Yang, *J. CO₂ Util.* 6 (2014) 17–25.
- [29] J.C. Wang, L. Zhang, W.X. Fang, J. Ren, Y.Y. Li, H.C. Yao, J.S. Wang, Z.J. Li, *ACS Appl. Mater. Interfaces* 7 (2015) 8631–8639.
- [30] Y. He, L. Zhang, B. Teng, M. Fan, *Environ. Sci. Technol.* 49 (2015) 649–656.
- [31] W. Yu, D. Xu, T. Peng, *J. Mater. Chem. A* 3 (2015) 19936–19947.
- [32] G. Song, F. Xin, J. Chen, X. Yin, *Appl. Catal. A* 473 (2015) 90–95.
- [33] M. Li, L. Zhang, X. Fan, Y. Zhou, M. Wu, J. Shi, *J. Mater. Chem. A* 3 (2015) 5189–5196.
- [34] X.J. She, J.J. Wu, H. Xu, J. Zhong, Y. Wang, Y.H. Song, K.Q. Nie, Y. Liu, Y.C. Yang, M.F. Rodrigues, R. Vajtai, J. Lou, D.L. Du, H.M. Li, P.M. Ajayan, *Adv. Energy Mater.* 7 (2017) 1700025.
- [35] S.G. Meng, X.F. Ning, T. Zhang, S.F. Chen, X.L. Fu, *Phys. Chem. Chem. Phys.* 17 (2015) 11577–11585.
- [36] J.G. Yu, S.H. Wang, J.X. Low, W. Xiao, *Phys. Chem. Chem. Phys.* 15 (2013) 16883–16890.
- [37] Z.X. Deng, C. Wang, X.M. Sun, Y.D. Li, *Inorg. Chem.* 41 (2002) 869–873.
- [38] J.J. Jang, C. Yu, S. Choi, S. Ji, E. Kim, J. Lee, *J. Catal.* 254 (2008) 144–155.
- [39] L. Nasi, D. Calestani, T. Besagni, P. Ferro, F. Fabbri, F. Licci, R. Mosca, *J. Phys. Chem. C* 116 (2012) 6960–6965.
- [40] J. Liu, Z. Guo, F. Meng, T. Luo, M. Li, J. Liu, *Nanotechnology* 20 (2009) 125501.
- [41] J. Ding, Z. Dai, F. Qin, H.P. Zhao, S. Zhao, R. Chen, *Appl. Catal. B* 205 (2017) 281–291.
- [42] X. Jia, M. Tahir, L. Pan, Z.F. Huang, X.W. Zhang, L. Wang, J.J. Zou, *Appl. Catal. B* 198 (2016) 154–161.